Monthly Notices
of the
ROYAL ASTRONOMICAL SOCIETY

MNRAS **437,** 2249–2262 (2014)
Advance Access publication 2013 November 22

doi:10.1093/mnras/stt2032

Multiwavelength diagnostics of the precursor and main phases of an M1.8 flare on 2011 April 22

A. K. Awasthi,[1]★ R. Jain,[1] P. D. Gadhiya,[1] M. J. Aschwanden,[2] W. Uddin,[3] A. K. Srivastava,[3] R. Chandra,[4] N. Gopalswamy,[5] N. V. Nitta,[2] S. Yashiro,[5] P. K. Manoharan,[6] D. P. Choudhary,[7] N. C. Joshi,[3] V. C. Dwivedi[6] and K. Mahalakshmi[6]

[1] *Physical Research Laboratory, Ahmedabad 380009, India*
[2] *Lockheed Martin Solar and Astrophysics Laboratory, Palo Alto, CA 94304, USA*
[3] *Aryabhatta Research Institute of Observational Sciences, Nainital 263129, India*
[4] *Department of Physics, DSB Campus, Kumaun University, Nainital 263002, India*
[5] *NASA Goddard Space Flight Center, Greenbelt, MD 20771, USA*
[6] *Radio Astronomy Centre, NCRA, TIFR, Ooty 643001, India*
[7] *California State University Northridge, Northridge, CA 91330-8268, USA*

Accepted 2013 October 21. Received 2013 August 26; in original form 2013 March 21

ABSTRACT

We study the temporal, spatial and spectral evolution of the M1.8 flare, which occurred in the active region 11195 (S17E31) on 2011 April 22, and explore the underlying physical processes during the precursor phase and their relation to the main phase. The study of the source morphology using the composite images in 131 Å wavelength observed by the Solar Dynamics Observatory/Atmospheric Imaging Assembly and 6–14 keV [from the *Reuven Ramaty High Energy Solar Spectroscopic Imager (RHESSI)*] revealed a multiloop system that destabilized systematically during the precursor and main phases. In contrast, hard X-ray emission (20–50 keV) was absent during the precursor phase, appearing only from the onset of the impulsive phase in the form of foot-points of emitting loops. This study also revealed the heated loop-top prior to the loop emission, although no accompanying foot-point sources were observed during the precursor phase. We estimate the flare plasma parameters, namely temperature (T), emission measure (EM), power-law index (γ) and photon turn-over energy ($\epsilon_{\rm to}$), and found them to be varying in the ranges 12.4–23.4 MK, 0.0003–0.6 $\times$ 10^{49} cm^{-3}, 5–9 and 14–18 keV, respectively, by forward fitting *RHESSI* spectral observations. The energy released in the precursor phase was thermal and constituted ≈1 per cent of the total energy released during the flare. The study of morphological evolution of the filament in conjunction with synthesized T and EM maps was carried out, which reveals (a) partial filament eruption prior to the onset of the precursor emission and (b) heated dense plasma over the polarity inversion line and in the vicinity of the slowly rising filament during the precursor phase. Based on the implications from multiwavelength observations, we propose a scheme to unify the energy release during the precursor and main phase emissions in which the precursor phase emission was originated via conduction front that resulted due to the partial filament eruption. Next, the heated leftover S-shaped filament underwent slow-rise and heating due to magnetic reconnection and finally erupted to produce emission during the impulsive and gradual phases.

Key words: conduction – Sun: filaments, prominences – Sun: flares – Sun: X-rays, gamma-rays.

1 INTRODUCTION

According to the 'standard model' of energy release in solar flares, the acceleration of the charged particles takes place following the reconnection of the overlying magnetic field lines. These accelerated electrons lose most of their energy through Coulomb collisions in the chromosphere and emit thick-target hard X-rays (HXRs). As a consequence, the chromosphere is heated up, which enhances the local pressure and thereby drives the heated plasma upwards into the coronal loops which appear in the form of soft X-rays (SXRs) as a

★ E-mail: arun.awasthi.87@gmail.com

result of thermal bremsstrahlung within the loop plasma. Following this mechanism, non-thermal emission (mostly in the HXR energy band) must either accompany or precede the SXR thermal emission (Shibata 1999; Jain et al. 2000, 2005, 2011; Shibata & Magara 2011). However, Markeev et al. (1983) showed the appearance of a pre-maximum phase a few minutes before the impulsive phase, termed later as the precursor phase and studied by several authors e.g. Fárník & Savy (1998), Veronig et al. (2002), Battaglia, Fletcher & Benz (2009), Falewicz, Siarkowski & Rudawy (2011), Awasthi & Jain (2011) and Altyntsev et al. (2012).

Based on multiwavelength observations, the time evolution of solar flare has been categorized into three phases, namely precursor, impulsive and gradual. Although the impulsive and gradual phases (combinedly termed as the main phase) of solar flares have been studied in greater detail, the underlying processes of energy release in the precursor phase and their relation to the main phase have not been fully established owing to the lack of high spatial, spectral and temporal resolution observations during the precursor phase. Further, the physical processes occurring during the precursor phase emission do not form a part of the standard model of energy release in solar flares (Shibata 1999; Shibata & Magara 2011) and therefore leave a missing link in the understanding of energy release processes during this phase. The aim of the current investigation is to understand the energy release process in the precursor phase and its association with the main phase.

The precursor to the flare is identified based on the disc-integrated X-ray emission (Fárník & Savy 1998). The precursor phase study with spatially resolved observations revealed interesting insights on the physical processes occurring during this phase and their relation to the main phase. From the spectral analysis of X-ray emission during the precursor phase, Battaglia et al. (2009) found that the precursor emission is of thermal origin and suggested that chromospheric evaporation during this phase occurs due to the conduction-driven saturated heat flux. On the contrary, Altyntsev et al. (2012), in their study of precursor events, used microwave observations and found the evidence of non-thermal electrons during this phase even when the HXR emission is absent. They suggested microwave observations to be better proxy of non-thermal processes during solar flares than the HXRs. Falewicz et al. (2011) found that the energy required to produce precursor SXR emission can be completely derived from the energy available with non-thermal electrons while discarding the need of any other heating mechanism. However, their analysis is constrained to a single-loop model. Therefore different schools of thoughts are being proposed to explain the origin of precursor phase emission. Further, in search of a driver of the instability during the precursor phase, Chifor et al. (2006, 2007) found slow-rise of the filament that is temporally and spatially associated with the precursor brightening (see also Joshi et al. 2011). Therefore, the origin of the precursor phase and its relation to the main phase has been an open issue, and a quantitative study of the thermal and non-thermal energetics as well as the filament dynamics employing multiwavelength observations is very essential.

During solar flare energy release, both the thermal and non-thermal emissions are usually observed (Jain et al. 2000, 2005). The non-thermal emission is an indication of the particle acceleration, while the thermal emission is a signature of chromospheric heating produced either by the non-thermal charge particle beam-driven plasma or by the conduction-driven plasma (Fisher, Canfield & McClymont 1985; Fisher 1989; Brosius & Holman 2012). Nishio et al. (1994), in their study of thermal and non-thermal energetics of solar flare using radio and SXR observations, found that the heated plasma observed during the impulsive and gradual phases can only be maintained from continuous bombardment of accelerated charge particles for ∼1000 s. Jain (1985) conducted the statistical study of 1885 Hα flares associated with microwave emission and suggested that two-ribbon flares and associated impulsive microwave bursts are produced as a consequence of the interaction of non-thermal electrons with the ambient plasma embedded in the strong magnetic field near lower atmosphere. Using *Solar Dynamics Observatory*/Atmospheric Imaging Assembly (*SDO*/AIA) observations, Brosius & Holman (2012) found that chromospheric evaporation is driven via thermal conduction front which is energized by magnetic reconnection. Li, Berlicki & Schmieder (2005) analysed spectral observations from the *Reuven Ramaty High Energy Solar Spectroscopic Imager* (*RHESSI*) and found that during the gradual phase, only 20 per cent of the energy transported to the chromosphere has been contributed due to the non-thermally accelerated charged particles; however, the rest came from the charged particles driven through thermal conduction. Radziszewski, Rudawy & Phillips (2011) performed a correlation study on Hα observation of high cadence with the respective X-ray emission and suggested that longer time-delays between Hα and HXR emissions of ≈20 s correspond to a slow chromospheric response associated with heating through conduction, whereas short delays ≈1–2 s are consistent with energy transfer through beam-driven evaporation. Accordingly, a correlation study of Hα and X-ray emissions provides a better opportunity to understand the principle mechanisms of energy transfer in various phases of solar flares. Therefore the spatial, spectral and temporal evolution of thermal and non-thermal sources is the focus of the current study in order to understand the underlying physical processes of energy release in various phases of emission.

Here, we present the investigation of spatial, spectral and temporal characteristics in various phases of the flare using multiwavelength observations during the M1.8 flare observed on 2011 April 22. We give a brief description of the observations used for this study in Section 2. Multiwavelength diagnostics of the precursor and main phases in conjunction with the morphological evolution of the filament are presented in Section 3. We discuss and summarize the study in Section 4.

2 OBSERVATIONS

The active region (AR) 11195 located at (S17, E31) on 2011 April 22 first appeared at the south-east limb on 2011 April 19. It produced six flares of Geostationary Operational Environmental Satellite (GOES) C-class and two M-class during 2011 April 20–22. The M1.8 flare that occurred on 2011 April 22 is the subject of the current investigation because this event shows very clear precursor enhancement before the impulsive phase as observed in multiwavelength emissions. In order to investigate the various phases of the flare, we use X-ray observations in 4–6 keV during 04:00:00–05:10:00 UT from the Si pin detector on board the *Solar X-Ray Spectrometer* (*SOXS*) mission. *SOXS* was launched on board the Indian *GSAT*-2 spacecraft on 2003 May 8 (Jain et al. 2005) and has been successfully operational till 2011 May 2. *SOXS* employs Si and CZT solid-state detectors to observe the Sun for 2–3 h every day. The Si detector provides high spectral resolution (∼0.8 keV) in the 4–25 keV energy range. The temporal cadence of observations is 3 s for the quiet activity time which, however, records the X-ray emission with the observing cadence of 100 ms during flare activity for 287 s based on the onboard automatic flare detection algorithm after which the observation cadence is returned to 3 s. The data have been archived on the *SOXS* URL http://www.prl.res.in/∼soxs-data. In addition, we use X-ray observations made by the *RHESSI* mission

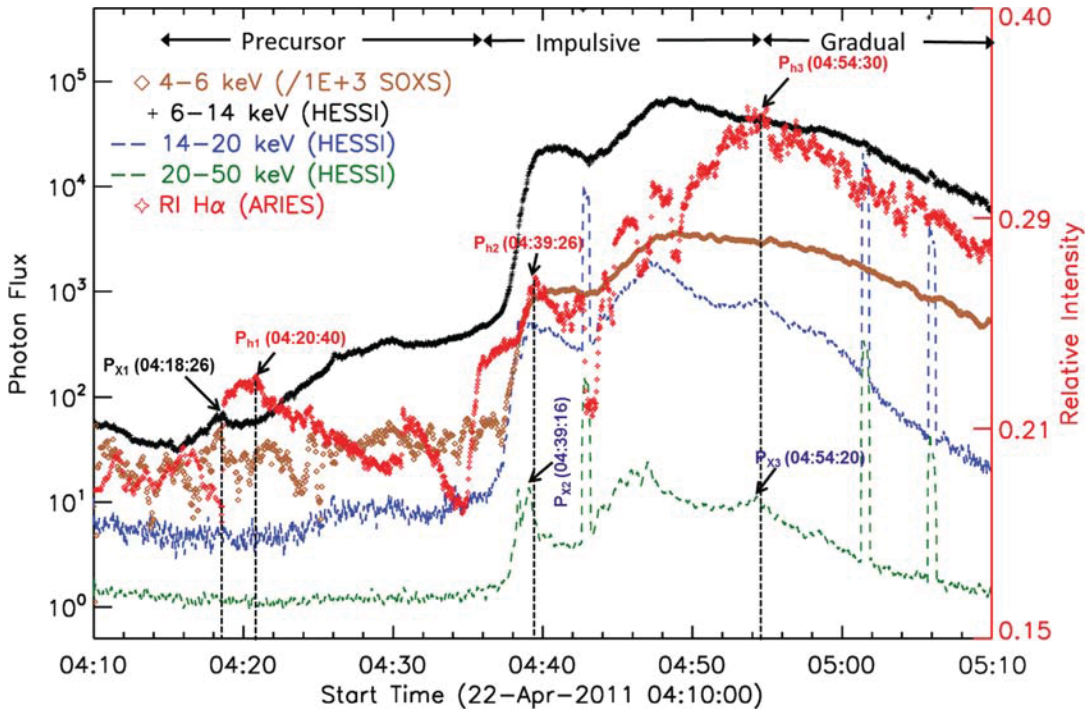

Figure 1. Temporal evolution of multiwavelength emission during M1.8 flare on 2011 April 22. Relative intensity estimated from Hα observations from ARIES/Nainital is plotted by the red coloured symbol. 4–6 keV emission observed by *SOXS* as well as 6–14, 14–20 and 20–50 keV emission by *RHESSI* are shown by the brown, black, blue and green symbols, respectively. $P_{x1,\,2,\,3}$ and $P_{h1,\,2,\,3}$ represent the corresponding peaks during precursor, impulsive and gradual phases in X-ray and Hα, respectively.

Table 1. Time line of activities during the precursor and main phases of the flare.

No.	Time (UT)	Observations/events
1	04:12:34–04:13:50	Eruption of the south-west leg (L1) of the filament
2	04:15:18	Onset of the precursor phase in 4–6 and 6–14 keV emission
3	04:18:26	First SXR peak during the precursor phase (P_{x1})
4	04:20:40	First Hα peak during the precursor phase (P_{h1})
5	04:27:14–04:36:00	Heating in the vicinity of the filament and enhanced ambient density
6	04:35:00	Onset of the filament eruption
7	04:36:00	Onset of impulsive phase in 20–50 keV (HXR) emission
8	04:39:16/04:39:26	First peak in HXR and RI in Hα time profile after onset of impulsive phase represented in Fig. 1 by P_{x2} and P_{h2}, respectively
9	04:45:00	Hα plage brightening in the south-east of the AR 11195
10	04:54:20	Commencement of the gradual phase
11	04:54:30	Peak emission in Hα as denoted by P_{h3} in Fig. 1
12	05:14:00	End of the gradual/decay phase

in the 6–50 keV energy band from 04:09:00 to 05:05:00 UT as the observations were not available during 04:00:00–04:09:00 UT due to *RHESSI* night time. The *RHESSI* facilitates X-ray imaging as well as spectroscopy of solar flares (Lin et al. 2002). These observations are analysed with the help of SolarSoftWare (SSW), a software tool with a repository of codes and graphical user interfaces written in the interactive data language (IDL). Shown in Fig. 1 is the intensity time profile of the flare in 4–6 keV (*SOXS*) and in 6–20 as well as in 20–50 keV (*RHESSI*), revealing the precursor, impulsive and gradual phases. We note several spikes in the *RHESSI* light curve which correspond to the change of attenuators during the observations. The event history is summarized in Table 1.

In order to explore the spatial correlation of multiwavelength emission with photospheric magnetic-field observations, we use observations from Helioseismic Magnetic Imager (HMI; Scherrer et al. 2012) on board the *SDO* mission. It provides full-disc magnetograms at wavelength 6173 Å with the spatial resolution of 0.5 arcsec per pixel and temporal cadence of 45 s. We further use *Extreme Ultraviolet* (EUV) observations in 94 and 131 Å wavelengths observed from AIA (Lemen et al. 2012) onboard *SDO* combining with the *RHESSI* observations to restore the structure of the emitting source. The *SDO*/AIA observes the Sun in EUV lines, namely Fe XVIII (94 Å), Fe VIII, XXI (131 Å), Fe IX (171 Å), Fe XII, XXIV (193 Å), Fe XIV (211 Å), He II (304 Å) and Fe XVI (335 Å). The spatial and temporal resolutions of these observations are 0.6 arcsec per pixel and 12 s, respectively. We investigate the spatial evolution of temperature (T) and emission measure (EM) synthesized from EUV observations taken by *SDO*/AIA in six wavelength channels, namely 94, 131, 171, 193, 211 and 335 Å, which cover the temperature range of 0.6 to ∼16 MK.

We study the temporal evolution of Hα emission and spatial evolution of filament using observations from Solar Tower Telescope

installed at Aryabhatta Research Institute of Observational Sciences (ARIES), Nainital, India (Uddin, Chandra & Ali 2006). The 15 cm, *f*/15 Hα telescope observes ARs on the Sun with superb time cadence (up to 2 s). The images are recorded by a 16 bit 1K×1K pixel CCD camera system having a pixel size of 13 μm with a spatial resolution of 0.58 arcsec per pixel. This provides unique opportunity to investigate the correlation of temporal evolution of Hα with multiwavelength intensity in various phases of the flare.

3 EVOLUTION OF MULTIWAVELENGTH EMISSION IN THE PRECURSOR AND MAIN PHASES

The precursor phase is identified by the enhanced X-ray emission in SXR (<20 keV) 10–20 min prior to the onset of the impulsive phase. Fig. 1 shows the temporal evolution of multiwavelength emission during M1.8 flare on 2011 April 22. 4–6 keV emission observed by *SOXS* as well as 6–14, 14–20 and 20–100 keV emissions observed by *RHESSI* are shown by the brown, black blue and green symbols, respectively. The relative intensity of the Hα emission observed by the Hα telescope at ARIES/Nainital is estimated from the following equation:

$$\mathrm{RI} = (I_\mathrm{f} - I_\mathrm{b})/I_\mathrm{b}.$$

Here, I_b represents the background intensity estimated from a 10 × 10 pixel rectangle away from the flare location and I_f represents the mean of the intensities of the region in the frame having intensities above I_b for respective frames. The temporal evolution of RI of Hα emission during the flare event is plotted by the red coloured symbol in Fig. 1. $P_{x1,2,3}$ and $P_{h1,2,3}$ represent the corresponding peaks during precursor, impulsive and gradual phases in the X-ray and Hα intensity profile, respectively.

From Fig. 1, we may note that the emission in the 4–6 and 6–14 keV energy band (from *SOXS* and *RHESSI* observations, respectively) has commenced on 04:15:18 UT and kept on increasing till 04:36:00 UT in the several steps. In contrast, the HXR (>20 keV) emission has been absent during the precursor phase while commenced at 04:36:00 UT in the form of impulsive burst almost simultaneous to impulsive SXR emission. Thus, we consider impulsive phase onset at 04:36:00 UT that lasted till 04:54:30, after which the gradual phase has commenced. The absence of the HXR emission in the precursor phase of this flare motivates us to probe the origin of the SXR emission. To understand this question, we study the spatial, spectral and temporal evolution of multithermal emission in various phases of the M1.8 flare occurred on 2011 April 22.

3.1 Spatial analysis

In order to study the spatial evolution of X-ray sources during the precursor and main phases, we synthesize X-ray images of the AR during the flare interval 04.08:30–05:05:30 UT on 2011 April 22 using *RHESSI* observations. *RHESSI* observes X-ray emission from the full solar disc in a wide energy range (3 keV to 17 MeV) with high temporal and energy resolution as well as with high signal sensitivity. Such observations enable us to synthesize the 2D images and spectra in the X-ray band, which provide valuable data for the investigation of topological evolution of the thermal and non-thermal sources during flares. We employ the CLEAN algorithm (Hurford et al. 2002) to synthesize the X-ray images during the precursor and main phases. Using the subcollimators 3F, 4F, 5F, 6F and 8F, the images are synthesized with the spatial resolution of 1 arcsec and integrated over 60 s duration in four energy bands, namely 6–10, 10–14, 14–20 and 20–50 keV. The purpose of synthesizing the images in the aforesaid energy bands is to study the morphological evolution of sources of thermal and non-thermal emission. Generally, 6–10 and 10–14 keV emissions are dominated by thermal processes. Further, 14–20 keV emission may be considered to be an intermediate-energy band between thermal or non-thermal processes and may be dominated by one component on the other over the evolution of the flare (Jain et al. 2005, 2011; Aschwanden 2007). However, >20 keV emission is considered to be originated mainly from the population of accelerated electrons and represents non-thermal source morphology. Further, in order to clearly visualize the source topology, we complement the synthesized X-ray images with the observations of *SDO*/AIA 131 Å. The temperature response of the 131 Å channel peaks ∼10 MK (Nitta et al. 2013) and therefore represents a very hot plasma produced during the flare heating due to thermal processes which are also the origin of SXR (<10 keV) emission. Fig. 2 shows a sequence of images in the 131 Å wavelength observed by *SDO* overlaid by the contours of 30, 50 and 80 per cent intensity (drawn by red, blue and yellow lines, respectively) of the maximum emission in the cotemporal 6–10 keV energy band during the precursor phase and main phases. Panel (a) of Fig. 2 shows 131 Å images at 04:09:09, 04:12:09 and 04:14:45 UT which represent the topology of AR and loops prior to the precursor phase commencement. We may note from panel (a) that the loop top appears to be brightened which may refer to the onset of heating at the coronal location of the loop and energizes the transfer of the coronal plasma towards the chromosphere through conduction. Panel (b) shows the precursor phase emission evolution at 04:18:33, 04:24:57 and 04:27:09 UT, respectively. Panel (c) shows the images at 04:31:09, 04:35:09 and 04:37:09 UT representing the topological changes during precursor to main phase emission changeover, and panel (d) represents the spatial evolution of sources during the main phase at 04:40:59, 04:47:00 and 04:55:00 UT. From panel (b), we may note a uniformly brightened loop 'L1' with a cusp-shaped structure. Further, from panels (c) and (d), it may be noted that as the impulsive phase has commenced, the loop which is brightened during the precursor phase has faded and another loop 'L2' located close to the northern foot-point of 'L1' started emission. From panel (d), we also note the systematic movement of X-ray emission as well as loops towards the north-west side. This kind of systematic motion in the SXR source appears to be associated with the phenomena of asymmetric eruption as already reported for an X2.6 event on 2005 January 15 by Liu et al. (2010).

Further, we present the evolution of 10–14, 14–20 and 20–50 keV (HXR) emissions during the precursor and main phase in Fig. 3. It is noteworthy that the X-ray intensity profile (cf. Fig. 1) did not show the emission in the HXR (>20 keV) energy band during the precursor phase which, however, has commenced at 04:36:00 UT, the onset of the impulsive phase. Panels (a), (b), (c) and (d) of Fig. 3 represent the *SDO*/AIA images in 131 Å wavelength at 04:25:45, 04:38:33, 04:47:00 and 04:55:49 UT, respectively, overlaid by contours of 30, 50 and 80 per cent of the intensities in 10–14, 14–20 and 20–50 keV drawn by red, blue and yellow coloured lines, respectively. It may be noted from panel (a) of Fig. 3, representing the images during the precursor phase at 04:23:45 UT, that we do not see any signature of foot-point emission. However, during the impulsive phase, as shown in panels (b) and (c), we note the foot-points as marked by 'f1' and 'f2'. Further, during the evolution of emission in the gradual phase, as shown in panel (d), the foot-point separation increases in comparison to that during the impulsive phase, which may suggest the rising of the reconnection region as modelled in Fletcher & Hudson (2001). Further, the source morphology in both 14–20 and

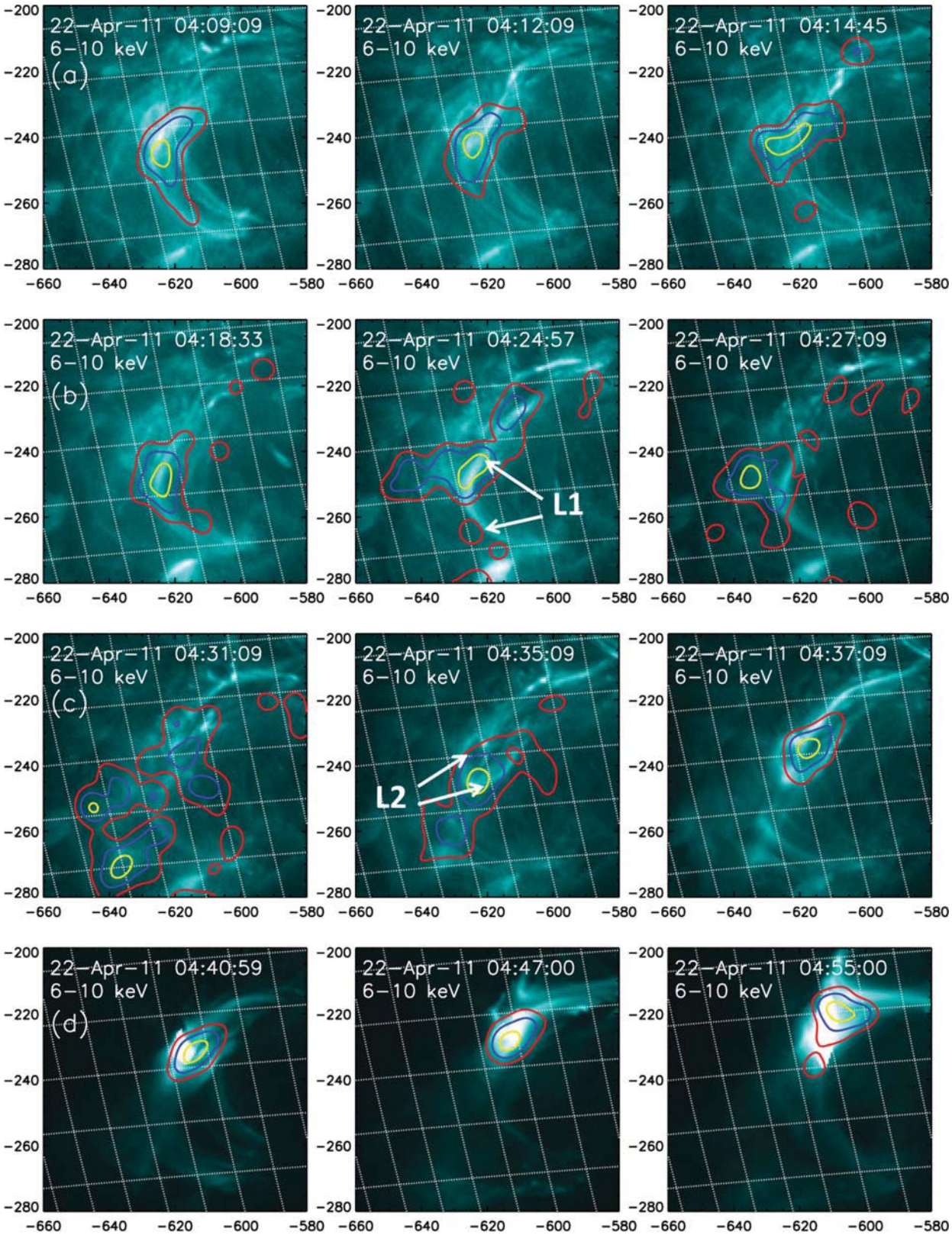

Figure 2. *RHESSI* X-ray contours of 30, 50 and 80 per cent intensity of the maximum of 6–10 keV energy band in each frame overplotted on the *SDO*/AIA observations in 131 Å wavelength. The three contours levels are drawn by the red, blue and yellow coloured lines, respectively. Panels (a) and (b) represent the evolution of thermal emission during the precursor phase, while (c) and (d) represent the same during precursor- to main-phase transition and main phase, respectively. The flaring loop during the precursor and impulsive phases is denoted by 'L1' in panel (b) and by 'L2' in panel (c), respectively.

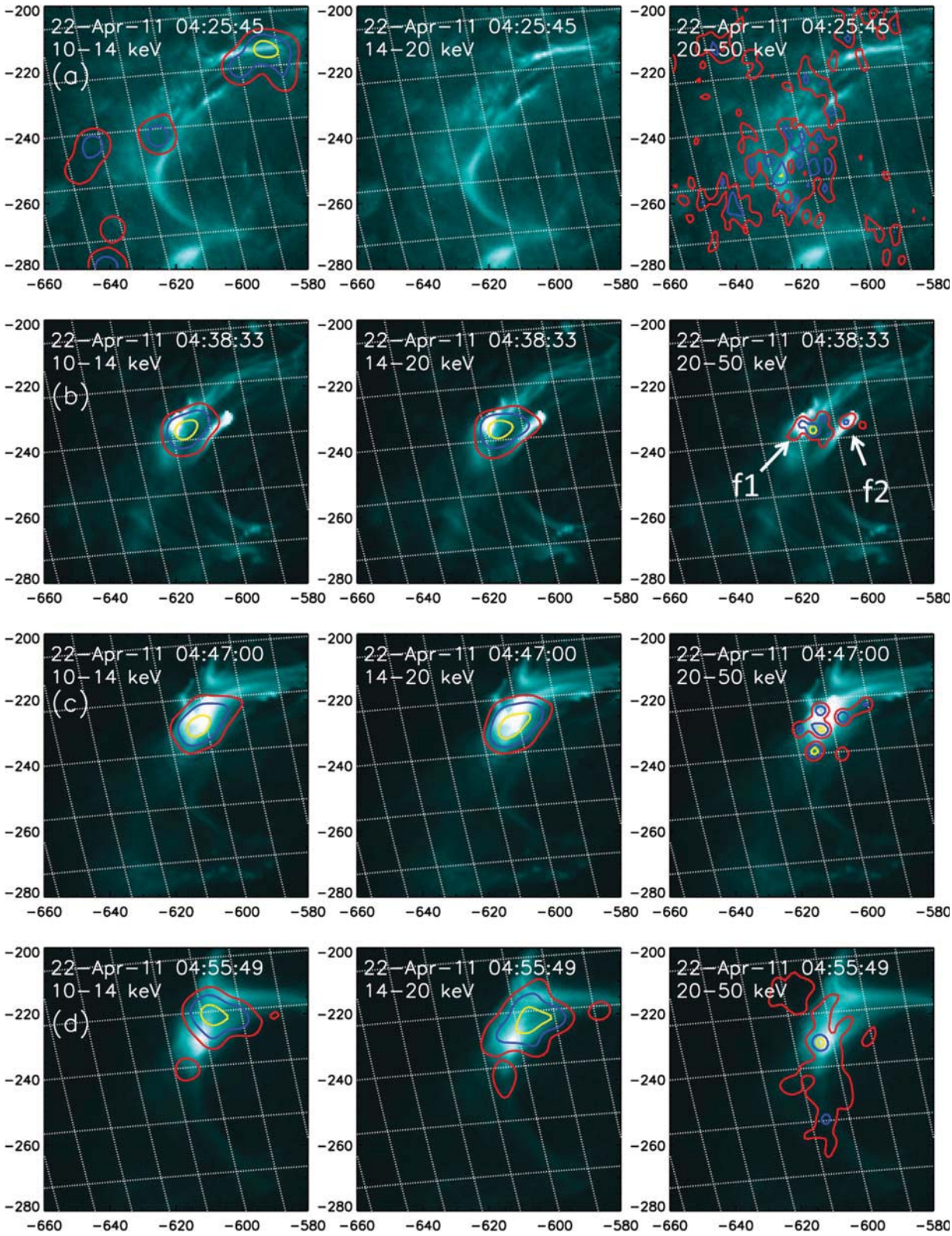

Figure 3. *RHESSI* X-ray contours of 30, 50 and 80 per cent intensity of the maximum of 10–14, 14–20 and 20–50 keV energy bands during the precursor and main phase overplotted on the 131 Å emission observations from *SDO*/AIA as shown from the top to bottom panels, respectively. The contours levels are drawn by red, blue and yellow blue coloured lines, respectively. The foot-points revealed by the X-ray images are denoted by 'f1' and 'f2'.

20–50 keV during the impulsive phase (panels b and c) reveals a foot-point-like structure which suggests that the 14–20 keV energy band is dominated by non-thermal emission during this phase of the flare.

3.2 Spectral and temporal evolution of the X-ray emission

We study the temporal evolution of the flare plasma parameters, namely temperature (T), emission measure (EM) and density (n_e)

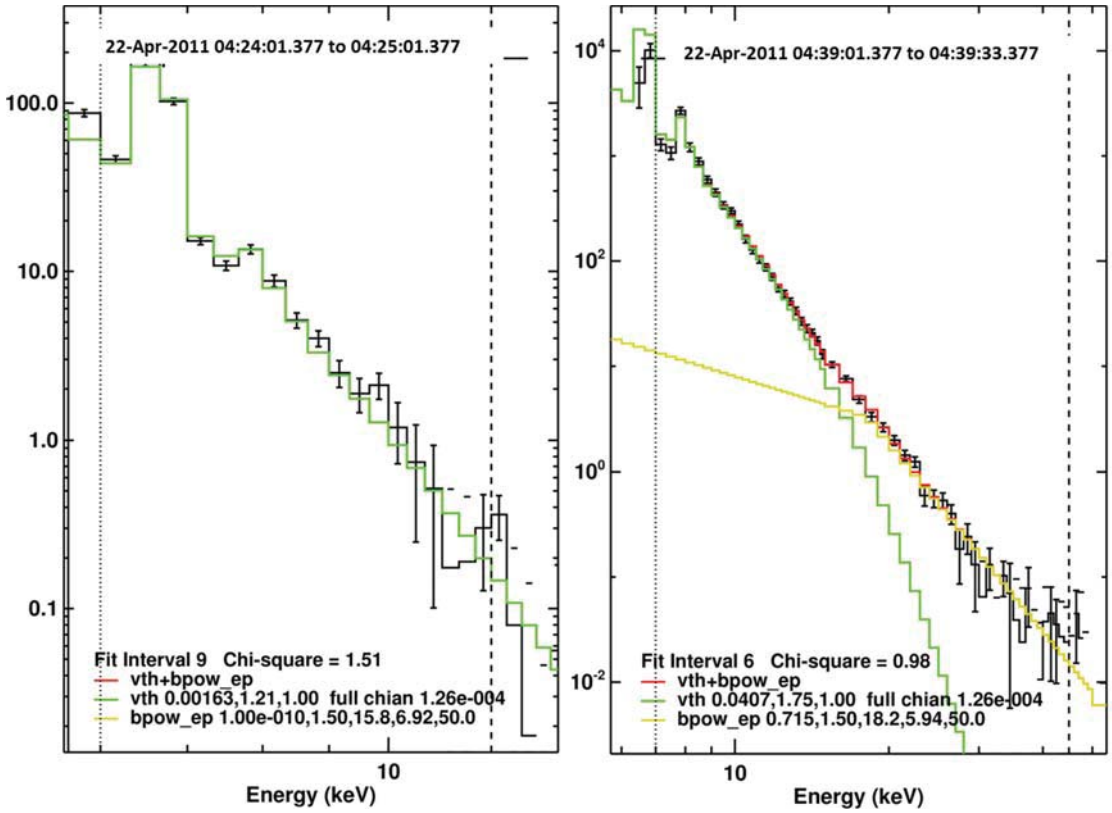

Figure 4. Photon flux spectrum of 2011 April 22 flare observed during 04:24:01–04-25:01 UT and 04:39:01–04:39:33 UT in the left- and right-hand panels, respectively, shown by the black line. The spectral fit in the left-hand panel is performed employing the isothermal photon model function (green line) and that in the right-hand panel employing isothermal (green line) + broken-power-law (yellow line) photon models with goodness of fit represented by $\chi^2 = 1.51$ and 0.98, respectively. The total model photon flux spectrum in the right-hand panel is shown by the red line.

employing the *RHESSI* observations. First, we synthesize the spectrum and spectral response matrix (SRM) files from the X-ray observations during 04:15:00 to 05:10:00 UT of 1 min and 32 s time cadence during the precursor and main phases, respectively. The energy resolution is kept to be 0.3 and 1 keV over the energy bands 6–15 and 15–50 keV, respectively. This spectrum and SRM files serve as input to the object spectral executive (OSPEX[1]) package provided in SSW. The OSPEX is an object-oriented interface for the X-ray spectral analysis of solar data. In each time bin, we used OSPEX to estimate the T, EM, power-law index by forward fitting the observed count spectra with the model count spectra generated by the in-built model functions, namely thermal, line emission, multithermal and non-thermal functions which use the CHIANTI data base (Dere et al. 1997; Landi et al. 2012). The SXR emission is originated either from the isothermal or multithermal plasma, while HXR emission is considered to be originated via non-thermally excited electrons (during reconnection). As there is no clear-cut demarcated energy between thermal and non-thermal emission, it is estimated by forward fitting the observed spectra simultaneously employing thermal and non-thermal model photon functions. The spectral fitting is carried out by iterative adjustment of the free parameters leading to χ^2 close to 1, which enable us to estimate the flare plasma parameters from the best fitting of modelled counts over the observed counts.

We obtained the best fit of the observed flux during the precursor phase considering the isothermal function. The left-hand panel of Fig. 4 shows the spectral fitting of the X-ray emission in the 6–15 keV energy band (shown by dotted lines) observed during 04:24:01–04:25:01 UT, the time of precursor emission. The observed photon flux spectrum (black line) is fitted with the isothermal model (green line) with the goodness of fit represented by $\chi^2 = 1.51$. The estimated temperature and emission measures are 1.21 keV (≈14 MK) and 0.0016×10^{49} cm^{-3}, respectively. The aforesaid technique is applied to the 1 min and 32 s integrated spectra during 04:15–04:36 UT and 04:36–05:10 UT, respectively, covering all phases of the flare. Thus, we estimated the temporal evolution of the temperature (T) and emission measure (EM) as shown in panels (a) and (b) of Fig. 6, respectively. We also show the evolution of density in panel (b) of Fig. 6. The density is estimated by employing the relation

$$n_e = \sqrt{\mathrm{EM}/V},$$

where EM is the emission measure and V is the volume of the flaring region. The temporal evolution of EM has already been estimated by forward fitting the observed spectra. As the loop morphology is very clear throughout the precursor and main phases, we estimate the volume using the cylindrical shape of the loops by $\pi r^2 l$ where r is the radius and l is the length of the flaring loop. The lengths of the loops have been estimated by manually tracing the same from the composite of the observation in 131 Å wavelength overlaid by contour of 30 per cent of the maximum intensity of the cotemporal 6–10 keV energy band and of 94 Å wavelength drawn by red and blue colours, respectively. The traced loop has been shown by light orange colour. The diameter of the traced loop is also calculated from these images by averaging the diameter estimated at three

[1] http://hesperia.gsfc.nasa.gov/ssw/packages/spex/doc/ospex_explanation.htm

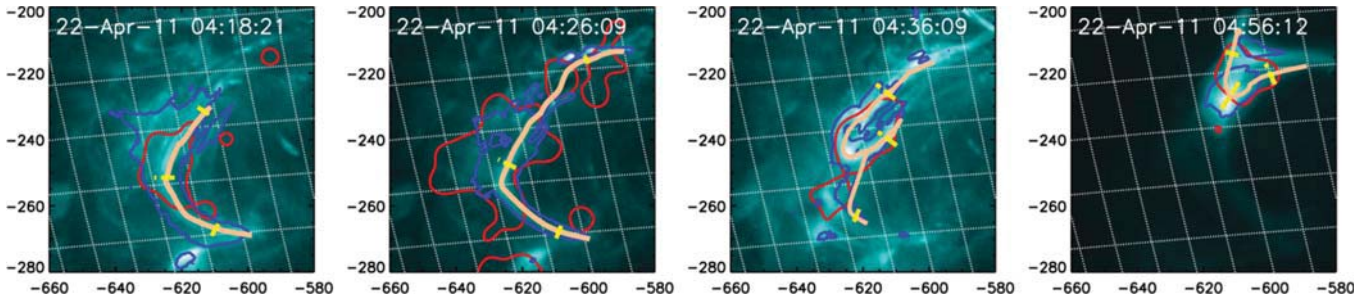

Figure 5. A sequence of images in 131 Å overlaid by contours of 30 per cent of the maximum intensity of cotemporal 6–10 keV energy band as well as in 94 Å wavelength drawn by red and blue colours, respectively. The traced loop is drawn by the light orange coloured line, while the diameter of the loop is shown by the yellow line.

different positions of the visible loop as drawn by the yellow line in Fig. 5. The first two images in Fig. 5 represent the shape of the loop during the evolution of emission in the precursor phase at 04:18:21 and 04:26:09 UT. The rest of the two images represent the loop topology during the impulsive phase at 04:36:09 and the gradual phase at 04:56:12 UT, respectively.

The non-thermal component in spectral observations during the impulsive phase is fitted considering the broken-power-law photon model function as shown by the yellow line in the right-hand panel of Fig. 4. The broken-power-law function provides us the photon turn-over energy ($\epsilon_{\rm to}$), power-law index (γ) above and below $\epsilon_{\rm to}$ and normalization value at 50 keV (F_{50}). The power-law index below $\epsilon_{\rm to}$ is fixed to the value of 1.5 (Saint-Hilaire & Benz 2005). The temporal evolution of the non-thermal power-law index (γ) and the HXR flux in 20–50 keV is plotted in panels (c) and (d) of Fig. 6, respectively. We find T, EM and γ to be varying in the range 12.4–23.4 MK, 0.0003–0.6 $\times$ 10^{49}cm^{-3} and 5–9.0, respectively. Further, the photon turn-over energy ($\epsilon_{\rm to}$) is found to be varying in the range 14–18 keV which is consistent with the similar X-ray source morphologies in the 14–20 and 20–50 keV energy bands as presented in Section 3.1. From the temporal evolution of the non-thermal power-law index (γ) (cf. panel d of Fig. 6), we may note that γ remains steady during the impulsive phase (04:47:10–04:54:30 UT) to the value of ∼7.0. This suggests continuous bombardment of non-thermally accelerated charged particles which may be noted from panel (d) of Fig. 6. We may further note the double peaks in the HXR intensity profile at 04:39:16 and 04:47:10 UT followed by a plateau region during 04:47:10–04:54:30 UT. This suggests the involvement of multiloop configuration followed by their systematic destabilization and activation which is consistent with the movement of the centroids of the X-ray as well as EUV 131 Å sources as revealed from the spatial study of multiwavelength sources in Section 3.1.

Further, this study has enabled us to perform a comparative study of the evolution of flare plasma parameters during the precursor and the main phase. The peak temperature during the precursor phase has been estimated to be 19.1 MK, ∼80 per cent of that attained during the impulsive phase (∼23.0 MK). It may be noted that the rate of increase of EM during the precursor phase has been insignificant in comparison to that during the impulsive phase. On the other hand, the estimated density has remained almost constant to the value of $\sim 10^{10}$ cm^{-3} during the precursor phase and increased rapidly after the commencement of the impulsive phase to the value $>10^{11}$ cm^{-3}. The above analysis shows slow evolution of T and $n_{\rm e}$ suggesting gradual heating during the precursor phase which is in agreement with Battaglia et al. (2009). This may also explain the absence of HXR foot-point emission. We further note from the temporal evolution of $n_{\rm e}$, as plotted in panel (b) of Fig. 6, that it again stabilizes just after the commencement of the gradual phase very similar to that during the precursor phase. This suggests the possibility of the common physical origin of the precursor and gradual phases dominated by thermal processes.

3.3 Thermal and non-thermal energetics

We estimate the thermal and non-thermal energies available during the precursor, impulsive and gradual phases of the flare evolution from the technique employed in Emslie et al. (2004, 2005) and Saint-Hilaire & Benz (2005). For estimating thermal energy, we employ

$$E_{\rm th} = 3k_{\rm b}T\sqrt{\rm EM \cdot\ V \cdot f} \qquad (1)$$

where T and EM represent the temperature and emission measure of flare plasma estimated from fitting the spectral observations in Section 3.2. V represents the volume of the flaring region and is estimated by the cylindrical approximation of the loops as discussed in Section 3.2. f represents the filling factor and is assumed to be 1 which gives an estimation of the upper limit of the thermal energy available in the flare. The thermal energy release rate is estimated to be varying in the range 0.1–4 $\times$ 10^{29} erg s^{-1}, as shown in Fig. 7. The total thermal energy released during the flare is estimated to be ∼1.3 $\times$ 10^{31} erg, out of which ∼2 per cent energy was released during the precursor phase and is estimated to be 2 $\times$ 10^{29} erg.

Further, we estimate non-thermal kinetic power considering the turnover model of electron flux as

$$P_{\rm nth} = \int_{E_{\rm min}}^{E_{\rm to}} A_e E_{\rm to}^{-\delta} {\rm d}E + \int_{E_{\rm to}}^{\infty} A_e E^{-\delta} {\rm d}E. \qquad (2)$$

Here, δ is the power-law index of the incident electron spectra and is estimated from the fitted power-law index γ by $\delta = \gamma + 1$. $E_{\rm min}$ is the minimum energy for the electron flux and considered to be 6 keV for the current study. $E_{\rm to}$ is the electron turn-over energy and estimated by the photon turn-over energy ($\epsilon_{\rm to}$) and electron power-law index (δ) employing the relation of fraction $\epsilon_{\rm to}/E_{\rm to}$ versus δ as derived in Saint-Hilaire & Benz (2005). They estimated that the fraction $\epsilon_{\rm to}/E_{\rm to}$ varies between 0.4 and 0.6 for the values of δ ranging from 3 to 8. With this relation, we estimate the interpolated value of the aforesaid fraction for each δ to estimate $E_{\rm to}$ corresponding to each $\epsilon_{\rm to}$. Thus, $E_{\rm to}$ is found to be varying in the range 24–35 keV. Further, A_e is obtained from the relation

$$A_\epsilon = \frac{A_e}{4\pi D^2}\overline{z^2}\frac{\kappa_{BH}}{K}\frac{B(\delta-2,1/2)}{(\delta-1)(\delta-2)},$$

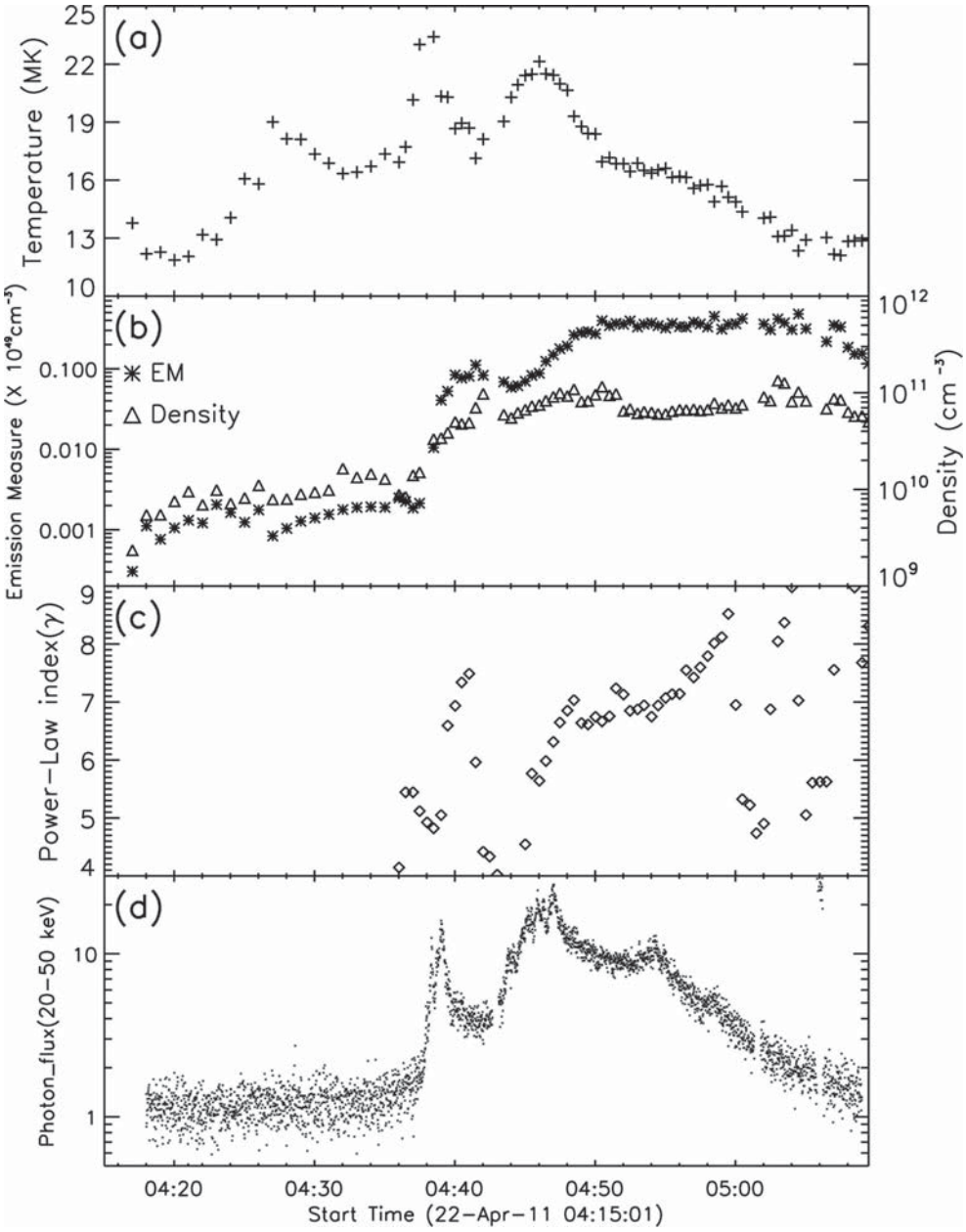

Figure 6. Panel (a): temporal evolution of temperature (T), panel (b): left – EM; right – density, panel (c): negative non-thermal power-law index (γ) and panel (d): intensity profile of emission in 20–50 keV from *RHESSI* observations.

where A_ϵ is the normalization index defined as

$$I_{\rm thick}(\epsilon) = A_\epsilon \epsilon^{-\gamma}.$$

The non-thermal kinetic power ($P_{\rm nth}$) for this flare is estimated which varies in the range 0.01–2 $\times$ 10^{30} erg s^{-1} and is shown in Fig. 8. Further, the total non-thermal energy released is estimated to be $\sim$4 $\times$ 10^{31} erg.

We perform a comparative study of the energy released during various phases of emission. The total (thermal+non-thermal) energy ($E_{\rm tot}$) released during the flare is estimated to be $\sim$5.3 $\times$ 10^{31} erg. During the precursor phase, only $\sim$1 per cent of $E_{\rm tot}$ has been released which is originating from thermal processes. Further, during the impulsive phase, the rate of release of non-thermal energy is dominated by that of thermal energy, and the fraction ($Q_{\rm f}$) of non-thermal to thermal energy release rate ($E_{\rm nth}/E_{\rm th}$) varies in the range 1–10 during this phase (cf. Fig. 7). However, after the onset of the gradual phase, the rate of release of non-thermal energy has been superseded by the thermal energy release rate and $Q_{\rm f}$ reduces to $\sim$0.2, in agreement with Li et al. (2005).

3.4 Temperature and emission measure evolution

We further study the spatial and temporal evolution of temperature (T) and emission measure (EM) employing multiwavelength observations. We synthesize T and EM maps using the technique established by Aschwanden et al. (2013). The T and EM maps over the AR are synthesized using observations from the six channels of EUV, namely 94, 131, 171, 193, 211 and 335 Å wavelengths. First, the alignment of the cotemporal images obtained in the six wavelengths with an accuracy of $\sim$1 pixel is performed by fitting

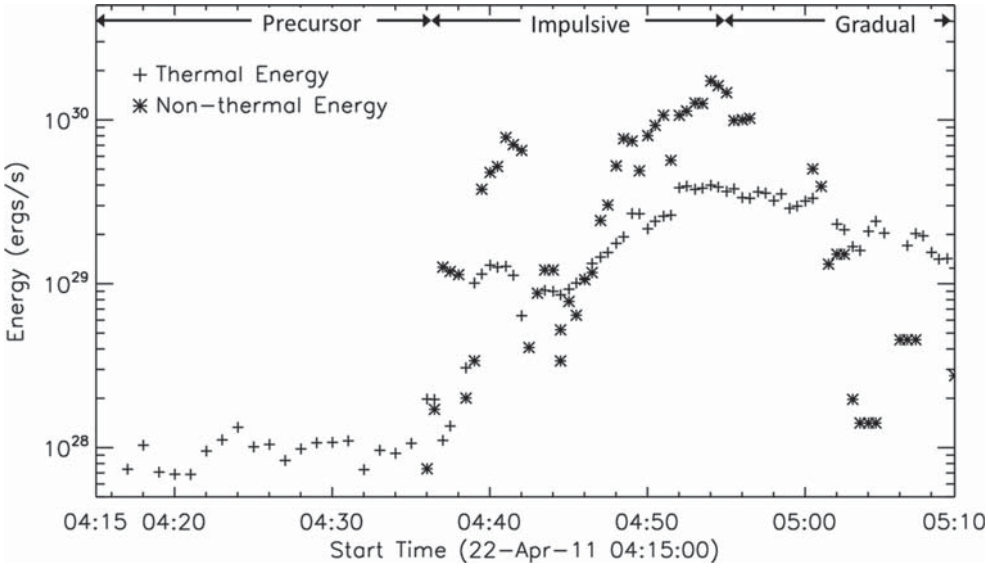

Figure 7. Temporal evolution of thermal and non-thermal energy release rate during various phases of the 2011 April 22 flare.

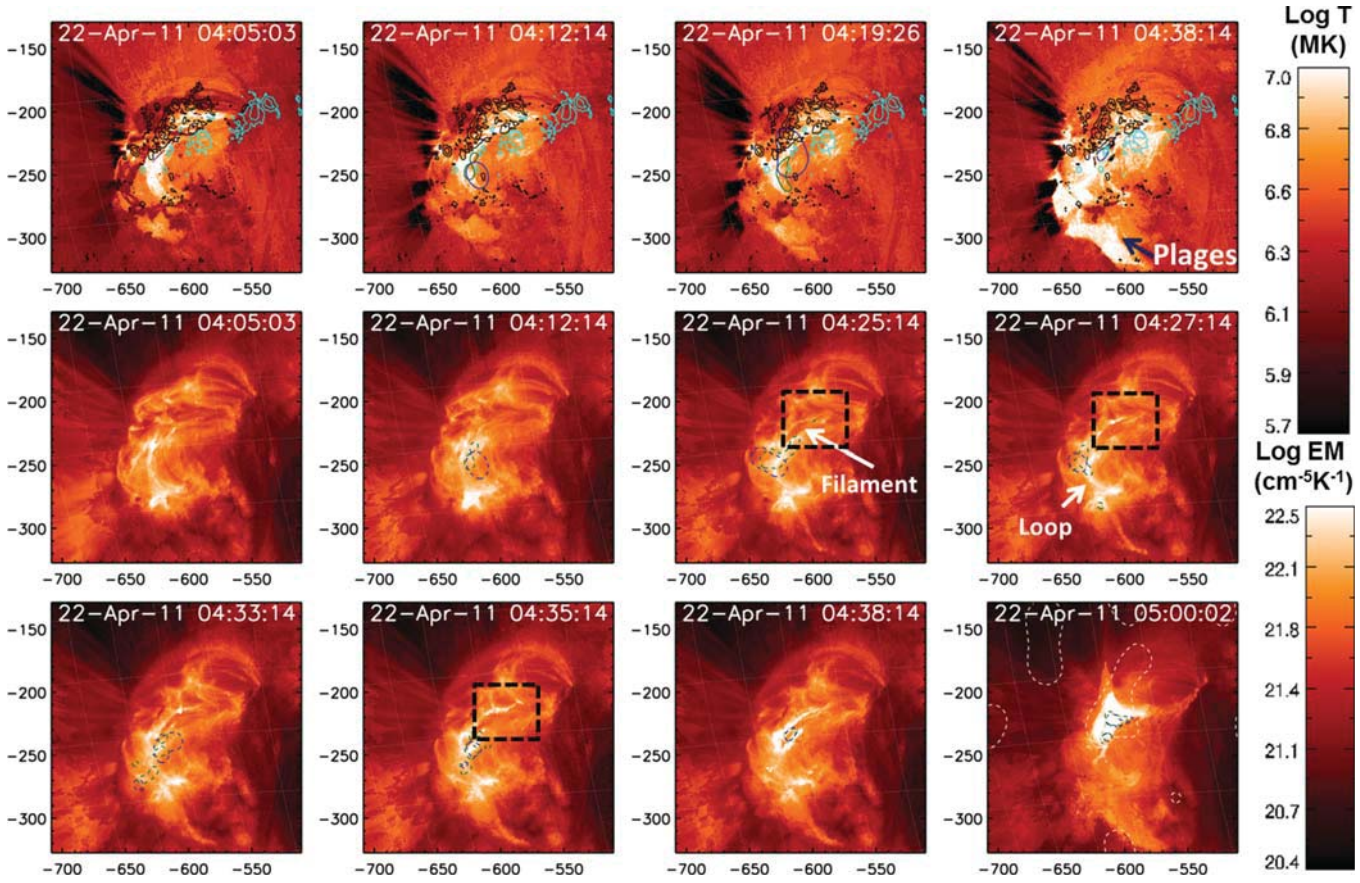

Figure 8. Temperature (top) and emission measure (middle and bottom panel) maps. The temperature map is overlaid by HMI contours of leading and following polarities as represented by cyan and black colours, respectively. The box in the middle and lower panels represent the region of enhanced intensity prior to the eruption of the filament.

the solar-limb detection algorithm.[2] The perfectly aligned images give a set of six EUV intensities at each pixel location over the AR which serves as input for forward fitting modelled by the Gaussian function to estimate the emission-measure-weighted temperature for a given pixel. This fitting is performed pixel-by-pixel to synthesize temperature and emission measure maps of the flaring region. We employ the aforesaid steps to the AIA observations obtained during 04:10:00–05:10:00 UT to synthesize the maps. The observations from *SDO*/AIA during the precursor phase were not saturated,

[2] http://www.lmsal.com/aschwand/software/aia/aia_dem.html

which allows us to restore the spatial evolution of T and EM without any limitation. Although the observations were saturated during the impulsive phase for some intermediate frames however, the automatic exposure control onboard *SDO*/AIA usually alternated between short and long exposure times during the flare and therefore every second image is unsaturated and avoids problems in synthesizing the T and EM maps. We estimate peak temperature in the duration of the synthesized map to be varying in the range 5.7–10 MK. We overlay the contours of 80 per cent of the maximum intensity of the 6–10, 10–14, 14–20 and 20–50 keV energy band on the T and EM maps as drawn by green, blue, khaki and light orange colour lines, respectively, as shown in Fig. 8. The top panel of Fig. 8 represents the spatial evolution of temperature at 04:05:03, 04:12:14, 04:19:26 and 04:38:14 UT, respectively. We further overlay the contour levels of 30 and 70 per cent of the maximum positive and negative magnetic-field observations from *SDO*/HMI over the T map to track the polarity inversion line (PIL). The contours corresponding to positive and negative magnetic fields are drawn with cyan and black lines, respectively. It may be noted from the T map synthesized at 04:05:03 UT that the heating has started cospatial to the PIL prior to the onset of SXR enhancement during the precursor phase. We further plot the EM map in the middle and bottom panels of Fig. 8 during the precursor and main phases, respectively.

The study of spatial evolution of the temperature with the time cadence of 12 s led us to various salient features: (1) the existence of a heated plasma cospatial to the PIL during the precursor phase; (2) heated area has been found to be substantially increased during the impulsive phase in comparison to that during the precursor phase and (3) plage brightening associated with the main phase with the peak temperature ∼10 MK. Similarly, from the synthesized EM maps we have been able to trace the filament location and morphological changes spatially associated with T and EM. Further, as previously mentioned, the loop-shape structure cospatial to the SXR contours visible during the precursor phase can be observed in the middle panel of Fig. 8. We have noticed enhanced density in the vicinity of the north-west leg of the filament first appeared at 04:27:14 UT as highlighted in the dashed box in the middle panel of Fig. 8. In addition, we have also noted the filament activity in the form of slow-rise prior to eruption, however, almost parallel to the line of sight of the observations imposing the restriction on estimating the speed of eruption. Further, it is noteworthy that the heated dense region has substantially enhanced at 04:35:14 UT, ∼60 s before the onset of impulsive phase emission. This suggests that the small-scale magnetic reconnection underneath the filament and associated heating have been going on prior to the accelerated eruption and the onset of impulsive phase of the flare. We further study the morphological evolution of the filament in conjunction with the synthesized T and EM maps in the following section.

3.5 Hα emission and filament morphology

We use Hα observations from ARIES/Nainital to study the role of the filament in the energy release during various phases of emission. Shown in Fig. 9 is a sequence of Hα images during various phases of emissions of the flare. The top panel shows a series of images representing the filament activity prior to the onset of the precursor phase at 04:01:15, 04:04:36, 04:05:52 and 04:10:54 UT, respectively. We denote the filament legs into the southern as well as eastern direction as L1 and L2, respectively. It may be noted that L1 started sequential movement towards east as marked in the top panel of the figure during 04:05:52–04:10:54 UT. Further, L1 possibly erupted prior to the onset of emission in the precursor phase and disappeared as may be seen in the frame at 04:15:05 UT in the middle panel. In addition to the partial eruption of the filament, we also noticed the filament activity in the form of sigmoidal shape and a clear appearance of the other leg during 04:29:48–04:36:00 UT as represented by L3 in the middle panel. The bottom panel of Fig. 9 represents the time sequence of Hα filtergrams during the main phase of the flare at 04:36:04, 04:37:45, 04:40:07 and 04:56:02 UT, respectively. We noted that the enhanced emission was visible at 04:37:45 UT, which expanded later during the gradual phase.

The study of the spatial evolution of the filament reveals the role of the partial filament eruption in triggering the precursor phase emission and later the whole filament system is destabilized prior to the onset of the main phase emission. In order to probe the cause of destabilization of the filament, we investigate the morphological evolution of filament in conjunction with the T and EM maps. Fig. 10 shows the time series of Hα observations from ARIES/Nainital overlaid by the contours of $\log T = 6.8$ and $\log \mathrm{EM} = 22.5$ drawn by red and green colours, respectively. We may note the heating of the filament from the top panel of Fig. 10, which represents the evolution of T and EM with Hα intensity during the precursor phase at 04:10:54, 04:18:28 and 04:29:48 UT, respectively. Further, the heating remains cospatially associated with the filament during the whole precursor phase which, however, followed an expansion during the main phase after the destabilization of the filament. In addition, contours representing EM evolution in the top panel clearly depict the loop-shaped structure during the precursor phase. The evolution of loop emission during the precursor phase has also clearly been visible in 131 Å emission.

4 SUMMARY AND CONCLUSIONS

We have investigated the spatial, spectral and temporal evolution of multiwavelength emission in various phases of the M1.8 flare occurred on 2011 April 22 in NOAA AR 11195. In this section, we combine the results obtained from multiwavelength analysis and interpretations to propose a unified scheme of energy release during the precursor and main phases. We present the key results of the study and associated implications as follows.

(i) The study of spatial evolution of multiwavelength emission during the precursor and main phases was performed. We note a brightened loop top in 131 Å observations prior to the onset of the precursor phase and later uniform loop emission during the precursor phase, whereas no foot-point emission was observed during this phase. Therefore, the appearance of coronal source heating prior to the precursor emission suggests the possibility of conduction-driven chromospheric heating during this phase. In contrast, the foot-point HXR sources in addition to the SXR loops were pronounced during the main phase emission which could be explained by the standard model of energy release in solar flares.

(ii) The spectral fitting was performed on the *RHESSI* observations over the flare duration to study the evolution of flare plasma parameters, namely temperature, emission measure and power-law index. The estimated temperature during the precursor phase attained its peak value of ∼19 MK in comparison to that in the impulsive phase of ∼23 MK. We also estimated the T and EM values from *SDO*/AIA observations. We note that the T values estimated from *RHESSI* were twice as high as those from *SDO*/AIA differential emission measure peak temperature. This difference in the temperature values might be attributed to the fact that the current investigation employs an isothermal photon function for estimating the flare plasma temperature from *RHESSI* observations which

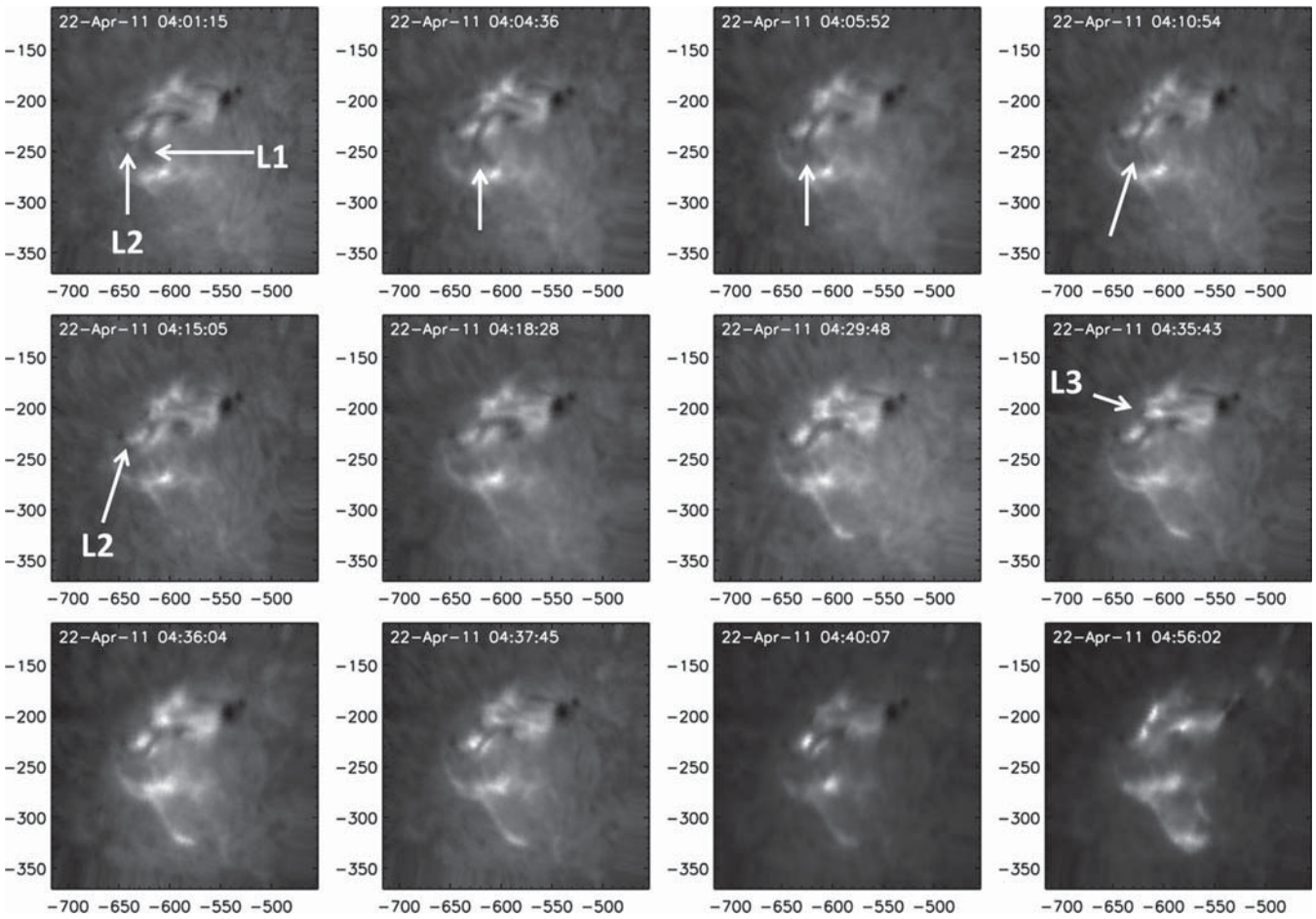

Figure 9. Top panel: sequence of images representing the filament activity prior to the onset of the precursor phase at 04:01:15, 04:04:36, 04:05:52 and 04:10:54 UT, respectively. Middle and bottom panels: evolution of filament during the precursor and main phases, respectively.

leads to the overestimated values of T as demonstrated in the recent studies by Ryan et al. (private communication) and Aschwanden & Shimiju (2013).

(iii) The spectral fitting also revealed that the rate of increase of EM during the precursor phase had been slow in comparison to that during the main phase. On the other hand, the estimated density (n_e) remained almost constant at $\sim 10^{10}$ cm^{-3} during the precursor phase, but increased drastically to $\sim 10^{11}$ cm^{-3} after the commencement of the impulsive phase. The temporal evolution of T and n_e suggests a relatively slow heating rate of the chromosphere most likely to be due to gentle evaporation by conduction front, which was also suggested by Battaglia et al. (2009).

(iv) The temporal evolution of density during the precursor and gradual phases did not show rapid changes in contrast to the evolution during the impulsive phase. This suggests that chromospheric evaporation is gradual in both phases. Earlier, Brosius (2009) also explored the scenario of gentle evaporation, however, only during the gradual phase.

(v) The study of the temporal evolution of the relative intensity of several Hα brightenings within the flaring region and its correlation with the X-ray emission was carried out. The onset of the precursor phase emission in Hα at 04:18:24 UT was unambiguous. Further, the first peak in the Hα emission P_{h1} was delayed by $\approx$134 s relative to that in 6–20 keV emission denoted by P_{x1}. Theoretically, the delay of the peak in Hα intensity profile with respect to the corresponding peak in the X-ray intensity profile represents the response time of the chromosphere which was heated either by the accelerated electrons or by the conduction front produced during magnetic reconnection. Considering the fact that this heating is produced by the non-thermal particles' interaction with the chromosphere, the delay was short ($\sim$10 s) which, on the other hand, turns out to be $\sim$20 s in the case of conduction-driven chromospheric evaporation (Radziszewski et al. 2011). The extraordinary long delay of 134 s might point towards the phenomena of slow response of the chromosphere undergoing through gentle evaporation originated by conduction front during the precursor phase. We estimated the half loop-length (L_{loop}) from the 131 Å image during the precursor phase to be $\sim$ 30 000 km, which, therefore, suggests the conduction front movement speed ($v_{cond} = L_{loop}/\Delta t$) to be $\sim$ 450 km s^{-1}. This estimated velocity might provide direct evidence to the numerically estimated speed of the conduction front ranging between 450 and 600 km s^{-1} by Guidoni & Longcope (2010). Further, during the impulsive phase, P_{h2} had been delayed by $\sim$10 s with respect to P_{x2}, which confirms the presence of non-thermal interaction with the chromosphere during this phase. The impulsive phase had shown two peaks at 04:39:16 UT (P_{x2}) and at 04:47:10 UT in HXR emission. Further, we might note a plateau region of HXR emission during 04:47:30–04:54:30 UT, which suggests the continuation of reconnection. Further, as the HXR emission is levelled off and the gradual phase onsets at 04:54:20 UT, third and the highest peak in Hα emission, denoted as P_{h3} in Fig. 1, at 04:54:30 UT appeared. This temporal comparison suggests that chromospheric heating due to non-thermal electrons started from the onset of the impulsive phase and continued until the plateau duration ended.

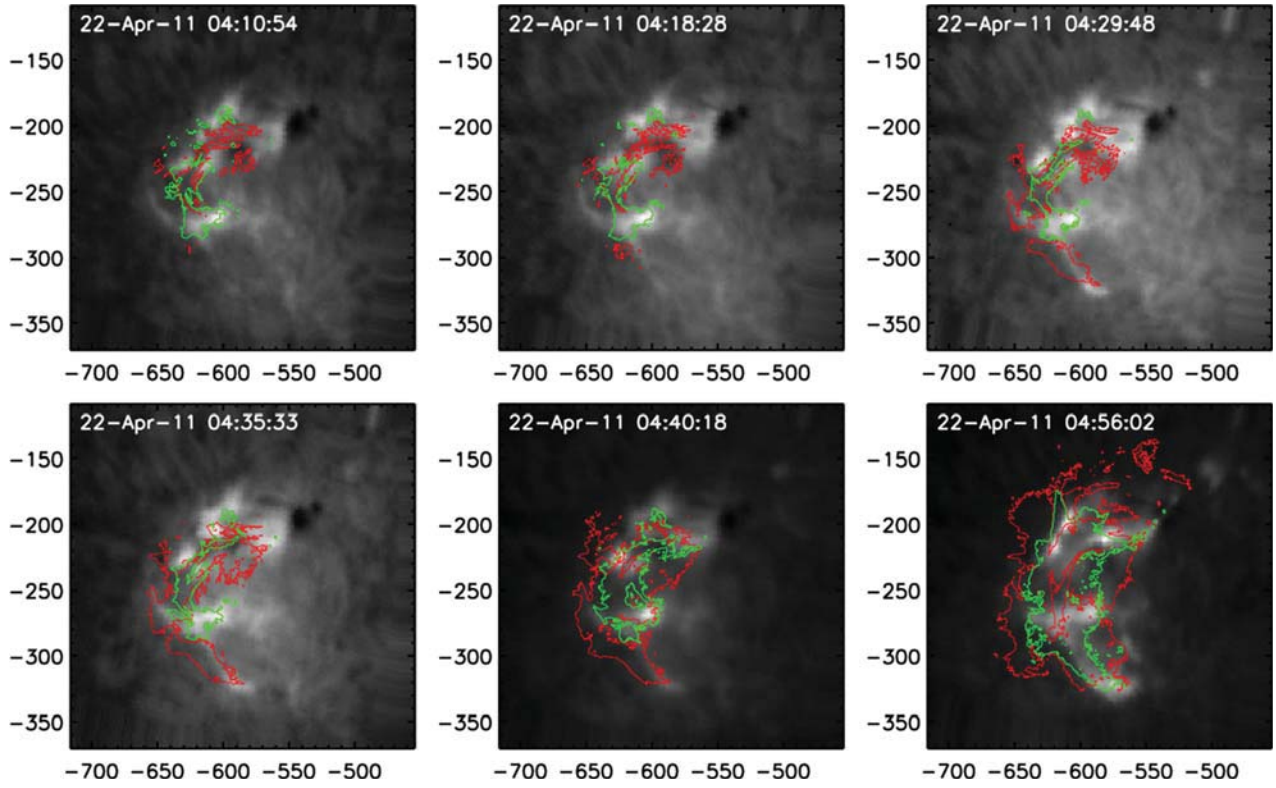

Figure 10. Sequence of Hα images (ARIES/Nainital) overlaid by the contours of log $T = 6.8$ and log EM $= 22.5$ drawn by red and green lines, respectively.

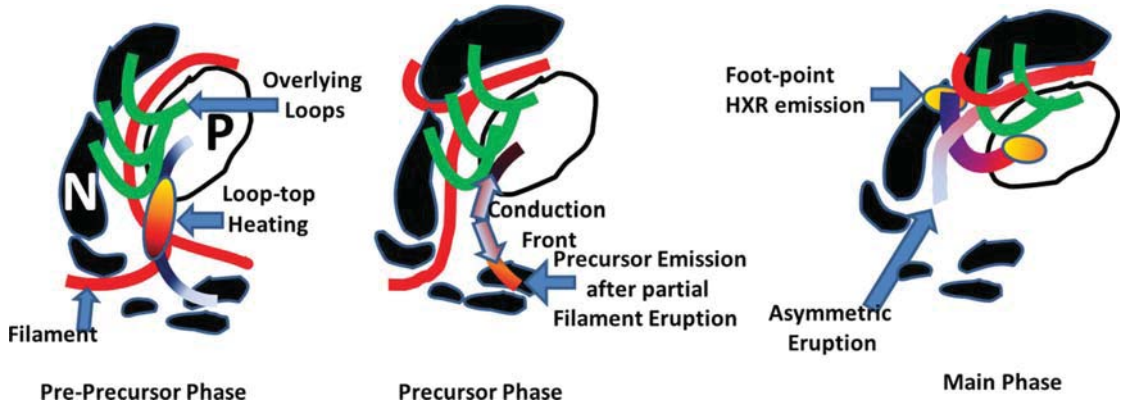

Figure 11. Schematics of the physical processes during the M1.8 flare from AR 11195. The filament is shown by the thick red line. The white blob (P) represents the positive polarity and the black scattered blobs (N) represent the negative polarities. The curves filled with gradient colours represent the emitting loops, while the green curves represent the overlying loops associated with the AR and the constituents of the main phase emission.

(vi) To understand the source of the energy made available during the precursor phase, we undertook the study of spatial evolution of T and EM in conjunction with the Hα filtergrams which revealed that the filament was heating up during the precursor phase. Further, we noticed the eruption of one leg of the filament L1 prior to the onset of the precursor phase. We also found slow movement in the filament leading to a sigmoid shape as well as an increase in the Hα intensity during the precursor phase.

(vii) This suggests that after the partial filament eruption leading to the precursor phase emission, the magnetic-field restructuring occurred which led to the more complex magnetic connectivity as depicted by the sigmoid-shaped filament. Thus, the filament underwent heating and slow-rise throughout the precursor phase caused by magnetic reconnection underneath the filament (Liewer et al. 2009) and the main phase emission was triggered by the eruption of the unstable filament. We also note the enhancement of EM in the vicinity of the north-east leg of the filament before the onset of filament eruption which assisted the scenario presented here for the eruption of the filament.

Based on the study and interpretations, we propose a unified scheme of energy release during the precursor and main phase emission in the flare event of investigation. Fig. 11 shows the schematics of the phenomenological evolution during the M1.8 flare of the current study. The filament is shown by the thick red line. The white blob (P) represents the positive polarity and the black scattered blobs (N) represent the negative polarities. The curves filled with gradient colours represent the emitting loops, while the uniform green curves represent the overlying loops associated with the AR and the constituents of the main phase emission. In this unified

scheme, the precursor phase emission originates via the conduction front triggered by the partial filament eruption. Next, the heated leftover S-shaped filament undergoes slow-rise and heating due to magnetic reconnection and finally erupts to produce emission during the impulsive and gradual phases.

ACKNOWLEDGEMENTS

The authors acknowledge the support of IUSSTF/JC-Solar Eruptive Phenomena/99-2010/2011–2012 project on 'Multiwavelength Study of Solar Eruptive Phenomena and Their Interplanetary Responses' to this study. They also acknowledge the free data usage policy of the *SDO*/AIA and *SDO*/HMI as well as *STEREO*, *SOXS* and *RHESSI* missions. AKA, RJ and PG acknowledge the support of Dept. of Space (Govt. of India). AKA and RJ acknowledge the guidance provided by Professor Brain Dennis during the *RHESSI* data analysis. The numerical computations have been performed on the three TFLOP clusters at PRL. This work is also a part of the project carried out under the Climate and Weather of the Sun-Earth System (CAWSES)-India programme supported by the Indian Space Research Organization (ISRO). The authors also acknowledge the support of the anonymous referee in the form of descriptive comments which helped in improving the manuscript.

REFERENCES

Altyntsev A. A., Fleishman G. D., Lesovoi S. V., Meshalkina N. S., 2012, ApJ, 758, 138
Aschwanden M. J., 2007, ApJ, 661, 1242
Aschwanden M. J., Shimiju T., 2013, ApJ, 776, 132
Aschwanden M. J., Boerner P., Schrijver C. J., Malanushenko A., 2013, Sol. Phys., 283, 5
Awasthi A. K., Jain R., 2011, in Choudhuri R. A., Banerjee D., eds, ASI Conf. Ser., Vol. 2, Multi-wavelength Diagnostics of Precursor Phase in Solar Flares. NCRA-TIFR, India, 297
Battaglia M., Fletcher L., Benz A. O., 2009, A&A, 498, 891
Brosius J. W., 2009, ApJ, 701, 1209
Brosius J. W., Holman G. D., 2012, A&A, 540, A24
Chifor C., Mason H. E., Tripathi D., Isobe H., Asai A., 2006, A&A, 458, 965
Chifor C., Tripathi D., Mason H. E., Dennis B. R., 2007, A&A, 472, 967
Dere K. P., Landi E., Mason H. E., Monsignori Fossi B. C., Young P. R., 1997, A&AS, 125, 149
Emslie A. G. et al., 2004, J. Geophys. Res.: Space Phys., 109, 10104
Emslie A. G., Dennis B. R., Holman G. D., Hudson H. S., 2005, J. Geophys. Res.: Space Phys., 110, 11103
Falewicz R., Siarkowski M., Rudawy P., 2011, ApJ, 733, 37
Fárník F., Savy S. K., 1998, Sol. Phys., 183, 339
Fisher G. H., 1989, ApJ, 346, 1019
Fisher G. H., Canfield R. C., McClymont A. N., 1985, ApJ, 289, 425
Fletcher L., Hudson H., 2001, Sol. Phys., 204, 69
Guidoni S. E., Longcope D. W., 2010, ApJ, 718, 1476
Hurford G. J. et al., 2002, Sol. Phys., 210, 61
Jain R., 1985, Bull. Astron. Soc. India, 13, 253
Jain R. et al., 2000, Bull. Astron. Soc. India, 28, 117
Jain R. et al., 2005, Sol. Phys., 227, 89
Jain R., Awasthi A. K., Rajpurohit A. S., Aschwanden M. J., 2011, Sol. Phys., 270, 137
Joshi B., Veronig A. M., Lee J., Bong S.-C., Tiwari S. K., Cho K.-S., 2011, ApJ, 743, 195
Landi E., Del Zanna G., Young P. R., Dere K. P., Mason H. E., 2012, ApJ, 744, 99
Lemen J. R. et al., 2012, Sol. Phys., 275, 17
Li H., Berlicki A., Schmieder B., 2005, A&A, 438, 325
Liewer P. C., de Jong E. M., Hall J. R., Howard R. A., Thompson W. T., Culhane J. L., Bone L., van Driel-Gesztelyi L., 2009, Sol. Phys., 256, 57
Lin R. P. et al., 2002, Sol. Phys., 210, 3
Liu C., Lee J., Jing J., Liu R., Deng N., Wang H., 2010, ApJ, 721, L193
Markeev A. K., Formichev V. V., Chertok I. M., Bhatnagar A., Jain R. M., Shelke R. N., Bhonsle R. V., 1983, Bull. Astron. Soc. India, 11, 318
Nishio M. et al., 1994, PASJ, 46, L11
Nitta N. V., Aschwanden M. J., Boerner P. F., Freeland S. L., Lemen J. R., Wuelser J.-P., 2013, Sol. Phys., 288, 241
Radziszewski K., Rudawy P., Phillips K. J. H., 2011, A&A, 535, A123
Saint-Hilaire P., Benz A. O., 2005, A&A, 435, 743
Scherrer P. H. et al., 2012, Sol. Phys., 275, 207
Shibata K., 1999, Ap&SS, 264, 129
Shibata K., Magara T., 2011, Living Rev. Sol. Phys., 8, 6
Uddin W., Chandra R., Ali S. S., 2006, J. Astrophys. Astron., 27, 267
Veronig A., Vršnak B., Dennis B. R., Temmer M., Hanslmeier A., Magdalenić J., 2002, A&A, 392, 699

This paper has been typeset from a TEX/LATEX file prepared by the author.